AGU PUBLICATIONS

Earth and Space Science

RESEARCH ARTICLE

10.1002/2014EA000043

Key Points:
- Presents a time-dependent, multistream hot electron transport model for Mars
- Conducted convergence tests of this model for closed magnetic field lines
- Validated the model's performance by examining several physical parameters

Correspondence to:
S. Xu,
xussui@umich.edu

Citation:
Xu, S., and M. W. Liemohn (2015), Superthermal electron transport model for Mars, *Earth and Space Science*, *2*, 47–64, doi:10.1002/2014EA000043.

Received 15 OCT 2014
Accepted 9 FEB 2015
Accepted article online 16 FEB 2015
Published online 14 MAR 2015

Superthermal electron transport model for Mars

Shaosui Xu[1] and Michael W. Liemohn[1]

[1]Department of Atmospheric, Oceanic, and Space Sciences, University of Michigan, Ann Arbor, Michigan, USA

Abstract This study presents a multistream superthermal electron transport model for the Mars space environment. This model includes the magnetic inhomogeneity effects, which is vital to understand electron motion around Mars. The convergence tests on the step sizes of variables are carried out and appropriate grid setups are determined. In addition, we have examined three physical parameters, $F_{10.7}$ values, thermal electron/plasma density, and neutral densities. Through the investigation of $F_{10.7}$ values, an interesting fact about the Hinteregger model is found that the photon flux of each wavelength is scaled differently. The resultant photoelectron fluxes also show a nonuniform percentage of increase. The results of plasma density and neutral densities tests are consistent with previous theories, such as the expected degradation of fluxes in the low-energy range with increased thermal electron/plasma density, and the elevated peak altitude of photoelectron fluxes with increased neutral densities. The examination of these physical parameters indicates the model's ability to simulate various environments and verifies the model's performance. Finally, a data-model comparison is carried out and the modeled omnidirectional fluxes agree well (within a factor of 2) with the observation.

1. Introduction

Superthermal electrons on Mars mainly consist of two parts: photoelectrons (due to the photoionization of the neutral atmosphere) and solar wind/magnetosheath electrons. These energetic yet still fairly low-energy (1–100 eV) electrons play an important role in the state and evolution of the Martian upper atmosphere, such as locally heating the atmosphere through collisions, causing optical emissions and ionization. While higher-energy electron precipitation (in the keV energy range) are rather inefficient at heating planetary upper atmospheres, superthermal electrons below 100 eV have a heating efficiency of 0.1 to 0.3 [e.g., *Torr et al.*, 1980; *Fox*, 1988], making them a critical energy source for ionospheres and thermospheres. Also, due to their high velocities, superthermal electrons are able to quickly transport energy from one place to another.

The modeling of electron transport through the Martian upper atmosphere has been carried out by previous investigators. Such efforts include the two-stream model [e.g., *Fox and Dalgarno*, 1979; *Rohrbaugh et al.*, 1979; *Seth et al.*, 2002], multistream models [e.g., *Mantas and Hanson*, 1979; *Haider et al.*, 1992; *Fox et al.*, 1993; *Fillingim et al.*, 2007], a simple analytic model [*Verigin et al.*, 1991], a kinetic and fluid model [*Leblanc et al.*, 2006], and an analytic yield spectrum approach [*Haider*, 1997; *Haider et al.*, 2002]. While these models have been very useful at providing insight into the electron transport at Mars, none of the aforementioned models include magnetic field gradients, which is vital to Martian plasma environment.

The strong crustal fields on Mars [*Acuña et al.*, 1998] makes its interaction with solar wind unique and more complicated than the usual unmagnetized planets. The resultant topology, i.e., draped, open, and closed magnetic fields, varies dramatically, geographically speaking, especially for the southern hemisphere [e.g., *Brain et al.*, 2003, 2007; *Krymskii et al.*, 2003; *Harnett and Winglee*, 2005; *Ma et al.*, 2014]. In addition, unlike Earth, the magnitude of the magnetic fields changes more rapidly within a few hundred kilometers in altitude. Hence, the model tool of the Martian environment requires a sophisticated theoretical description and the ability to modulate arbitrary magnetic fields.

The Mars Monte Carlo Electron Transport Code (MarMCET) [*Lillis et al.*, 2008, 2009], a kinetic, test particle approach to electron motion takes into account both the magnetic gradient and the anisotropic pitch angle distributions of the electrons. This model has been used, for example, to explore the Martian nightside ionosphere [*Lillis et al.*, 2009, 2011].

While MarMCET solves the Lorentz equation for each test particle, our multistream model takes a different approach, calculating the superthermal electron distribution function from the gyration-averaged

Boltzmann kinetic equation, and simulates the superthermal electron transport along a flux tube [*Liemohn et al.*, 2003]. It was initially developed for the Earth environment [*Khazanov et al.*, 1993; *Khazanov and Liemohn*, 1995; *Liemohn et al.*, 1997] and has then been modified for the Martian upper atmosphere [*Liemohn et al.*, 2003, 2006]. This model not only satisfies the aforementioned requirements to simulate electron transport in the Martian environment but also has the potential to model time-dependent processes.

Even though this superthermal electron transport (STET) model has already been used to simulate the Martian environment [*Liemohn et al.*, 2003, 2006], this study provides an extensive description of the model (section 2) and rigorous numerical convergence tests on the STET model (section 3). In addition, three physical parameters, $F_{10.7}$ values, thermal electron/plasma density, and neutral densities, are examined (section 4). These tests not only demonstrate the STET model's ability to handle a large range of inputs but also verify the performance of the model. In section 5, the final validation of the model is through the comparison between the model and the observations from the magnetometer/electron reflectometer (MAG/ER) instrument on board Mars Global Surveyor (MGS).

2. Methodology

Starting with the Bolzmann kinetic equation [*Khazanov et al.*, 1994, equation (1)], assuming that the electron Larmor radius of superthermal electrons is small compared to the gradient of the local magnetic field [*Liemohn et al.*, 2003], the guiding center approximated version in the coordinate system [t, E, μ, s] is expressed as

$$\frac{\beta}{\sqrt{E}}\frac{\partial\psi}{\partial t}+\mu\frac{\partial\psi}{\partial s}-\frac{1-\mu^2}{2}\left(-\frac{F}{E}+\frac{1}{B}\frac{\partial B}{\partial s}\right)\frac{\partial\psi}{\partial\mu}+EF\mu\frac{\partial}{\partial E}\left(\frac{\psi}{E}\right)=Q+S_{ee}+\sum_{\alpha}\left(S_{e\alpha}+S^{*}_{e\alpha}+S^{+}_{e\alpha}\right)+\sum_{i}\left(S_{ei}+S^{*}_{ei}+S^{-}_{ei}\right) \tag{1}$$

where, E is the electron energy in eV, s is the coordinate along the local magnetic field line, and θ is the electron pitch angle, the constant $\beta = 1.7\times10^{-8}eV^{1/2}$ cm^{-1} s, $\mu = \cos\theta$. The force due to a parallel electric field is $F = eE_{\parallel}$, in units of eV cm^{-1}. S_{ee} describes collisions with Maxwellian/thermal electrons, $S_{e\alpha}$ and S_{ei} elastic collisions with neutral and ion species, $S^{*}_{e\alpha}$ and S^{*}_{ei} account for excitation of neutral and ion species, $S^{+}_{e\alpha}$ and S^{-}_{ei} ionization and recombination, and Q the electron production rate due to photoionization of neutral species. $\psi(t, E, \mu, s)$ is the differential flux of electrons and $\psi dE d\Omega$ is the flux of electrons with energy from E to $E + dE$ inside a solid angle $d\Omega$ at a point s along the field.

Note that the use of a guiding center approximation for these calculations is justified because the gyroradius of the simulated electrons is always less than the radius of curvature of the field lines as well as less than the spatial grid step. For instance, the lowest magnetic field values used in the calculations below is 10 nT, which results in a gyroradius of 1 km and 3.4 km for 10 and 100 eV electrons, respectively. The magnetic field radius of curvature, for the fields applied in this study, are at a minimum 50 km and usually much larger than this. In addition, the step size used in these regions of low magnetic field will always be larger than the electron gyroradius within our simulation energy range.

Due to the much larger densities of neutral species than ions and the small cross section of dissociative recombination for superthermal electrons, the terms S^{*}_{ei} and S^{-}_{ei} are generally neglected. The rest of the collision terms can be expressed as

$$S_{ee}+S_{ei}=An_e\left\{\frac{\partial}{\partial E}\left(\frac{\psi}{E}\right)+\frac{1}{2E^2}\frac{\partial}{\partial\mu}\left[\left(1-\mu^2\right)\frac{\partial\psi}{\partial\mu}\right]\right\} \tag{2}$$

$$S_{e\alpha}=\frac{n_\alpha\sigma^{(1)}_\alpha}{2}\frac{\partial}{\partial\mu}\left[\left(1-\mu^2\right)\frac{\partial\psi}{\partial\mu}\right] \tag{3}$$

$$S^{*}_{e\alpha}=n_\alpha\sum_j\left[\sigma^{*}_{\alpha j}\left(E+E^{*}_{\alpha j}\right)\psi\left(E+E^{*}_{\alpha j},\mu\right)-\sigma^{*}_{\alpha j}(E)\psi(E,\mu)\right] \tag{4}$$

$$S^{+}_{e\alpha}=n_\alpha\int_{E+E^{+}_{\alpha}}^{2E+E^{+}_{\alpha}}I^{+}_{\alpha}\left(E',E'-E-E^{+}_{\alpha}\right)\psi(E',\mu)dE'+\frac{n_\alpha}{2\pi}\int_{2E+E^{+}_{\alpha}}^{\infty}I^{+}_{\alpha}(E',E)\int_0^{2\pi}\psi\left(E',\sqrt{1-\mu^2}\cos\eta\right)d\eta dE'-n_\alpha\sigma^{+}_{\alpha}(E)\psi(E,\mu) \tag{5}$$

where $A=2\pi e^4 \ln\Lambda = 2.6\times10^{-12}$ eV^2 cm^2, and $\ln\Lambda$ is the Coulomb logarithm, n_α is the density of neutral species α, $\sigma_\alpha^{(1)}(E)=\int I_\alpha(E,\chi)(1-\cos\chi)\mathrm{d}\Omega$ is the transport cross section, χ is the scattering angle, and $I_\alpha(E,\chi)$ the differential elastic cross section, $\sigma_{\alpha j}^*$ is the total cross section of scattering to excite a neutral particle with a threshold energy $E_{\alpha j}^*$, and the ionization energy is E_α^+. The total cross section of ionization by an electron with an energy E is

$$\sigma_\alpha^+(E) = \int_0^{(E-E_\alpha^+)/2} I_\alpha^+(E,E_2)\mathrm{d}E_2 \tag{6}$$

where $I_\alpha^+(E,E_2)$ is the appropriate differential cross section and E_2 is the energy of a secondary electron.

The detailed simplification of these collision terms are described in *Khazanov et al.* [1994]. In addition, terms of order of m_e/m_i, where m_e and m_i are the mass of electron and ions, respectively, and second derivatives with respect to energy are also omitted from the calculation [*Khazanov et al.*, 1994].

As said in section 1, the magnetic field magnitude on Mars can change by a factor of ten within a few hundred kilometers, which means a larger variation of the local pitch angle than found at Earth. To avoid a non-Cartesian grid, which may increase the approximation errors of the derivatives $\partial/\partial s$ and $\partial/\partial\mu$, the kinetic equation is rewritten in s-μ_0 space, instead of s-μ space. Here $\mu_0=\cos(\theta_0)$ and θ_0 is the pitch angle at the location of minimum B, also referred as minimum-B pitch angle. The transformation from the local pitch angle μ to the minimum-B pitch angle μ_0 is

$$\mu_0 = \frac{\mu}{|\mu|}\sqrt{1-\frac{B_0}{B}(1-\mu^2)} \tag{7}$$

where B_0 is the minimum B strength along the field line. Figure 7 of *Liemohn et al.* [2003] shows the corresponding s-μ_0 space to s-μ space, and a Cartesian grid is applicable with the removal of the $\partial B/\partial s$ term. With this new space, only slow collisional processes redistribute the electrons in μ_0.

The code was designed to well resolve the "slow" process of pitch angle scattering. Hence, equation (1) is rewritten as a diffusion equation in s-μ_0 space,

$$\left(\sqrt{\frac{m}{2E}}\frac{\partial\psi}{\partial t}+\mu\frac{\partial\psi}{\partial s}+C_1\frac{\partial\psi}{\partial E}\right)+C_2\frac{\partial}{\partial\mu_0}\left(C_3\frac{\partial\psi}{\partial\mu_0}\right)=Q \tag{8}$$

In equation (8), the coefficients C_1, C_2, and C_3 include summations over various neutral and plasma species in the Martian upper atmosphere. In equation (8), the spatial transport derivative (the second term) and the energy degradation derivative (the third term) are treated analogously as the time derivative in a standard diffusion equation, a numerical technique developed by *Khazanov* [1979]. By using a finite-difference approximation for these real/pseudotime derivatives,

$$\frac{\partial\psi}{\partial t}=\frac{\psi-\psi^{t-\Delta t}}{\Delta t} \tag{9}$$

$$\frac{\partial\psi}{\partial s}=\begin{cases}\frac{\psi-\psi^{-s}}{\Delta s} & \mu_0>0\\ \frac{\psi-\psi^{+s}}{\Delta s} & \mu_0<0\end{cases} \tag{10}$$

$$\frac{\partial\psi}{\partial E}=\frac{\psi^E-\psi}{\Delta E} \tag{11}$$

equation (8) can be reduced to

$$\frac{\partial^2\psi}{\partial\mu_0^2}+D_1\frac{\partial\psi}{\partial\mu_0}-D_2\psi=D_3. \tag{12}$$

where $\psi^{t-\Delta t}$ is ψ at the previous time step; ψ^{+s} and ψ^{-s} are ψ at the next upper and lower s step; ψ^E is the ψ at the next higher-energy step; Δt, ΔE, and Δs are the step lengths in t, E, and s. Coefficients D_1, D_2, and D_3 are functions of the variables t, s, μ_0, and E. More details of the derivation can be found in *Khazanov* [1979] and *Gefan and Khazanov* [1990].

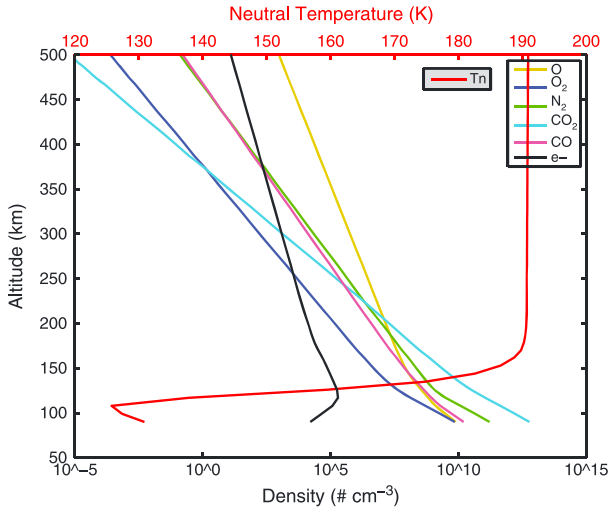

Figure 1. Neutral densities, thermal electron density, and neutral temperature of Mars to be used in the calculations that follow, from MTGCM against altitude.

The analogy of the spatial transport derivative and energy degradation derivative to the time derivative disadvantages the resultant scheme in resolving propagation fronts along the field line but well suits for resolving the long-term development, evolution, and interplay between the source cones and trapped zone [*Liemohn et al.*, 2003].

The last pitch angle (PA) grid of each spatial location requires a special formula for the calculation of the flux at this grid point, denoted as k_{end} [*Liemohn*, 1997]:

$$\psi_{k_{end}} = \left[\frac{\beta \psi^{t-\Delta t}}{\sqrt{E}\Delta t} + \frac{\mu \psi^{s-\Delta s}}{\Delta s} + \frac{\xi \psi^{E-\Delta E}}{\Delta E} + Q + S + \frac{p_{end}}{2}\left(\psi^{+}_{k_{end}-1} + \psi^{-}_{k_{end}-1} \right) \right] / \left(p_{end} + \frac{\beta}{\sqrt{E}\Delta t} + \frac{\mu}{\Delta s} + \frac{\xi}{\Delta E} + L \right) \quad (13)$$

where p_{end} stands for the fraction of the electron flux scattered from the pitch angle $k_{end}-1$, "+", and "−" superscripts upward and downward flowing flux, respectively. S here is the source due to cascading and L represents the energy degradation due to collisions. Finally, $\xi = An_e/E$, related to the Coulomb collision. At very low altitudes, the scattering terms with p_{end} dominates the numerator and denominator of this equation, resulting in a nearly isotropic distribution. At higher altitudes, either the Δt or Δs terms will dominate this equation. However, in our setup for these simulations with a very large Δt (i.e., jump to steady state), there is one exception. At the spatial location of minimum B, the local μ value for k_{end} is $\mu = 0$, and therefore, the transport terms drop to zero. This allows other, usually negligible, source terms to dominate the equation, which can result in an anomalously large flux value in this one point of the $s-\mu_0$ grid. To correct this issue, add some small transport to PA = 90°, as would be the case if some small perturbations were present. The specific implementation of this small transport effect is defined that $\mu(k_{end}, i) = (\mu(k_{end}-1, i) + \mu(k_{end}-1, i+1))/8$, where i indicates the spatial grid points.

The boundary conditions applied to STET are as follows. For the energy grid, it is assumed that the flux above the highest-energy step is zero. For the spatial grid, it is assumed that there is no source below the lowest-altitude step and that any downward directed flux at this location is lost. If the field line is "open" and connected to the solar wind at either or both ends, then the highest altitude spatial step will have an imposed downward directed electron flux and the upward fluxes are assumed to be lost.

The solar photon flux used in this study is from the *Hinteregger et al.* [1981] model as scaled by $F_{10.7}$, with the additional correction from *Solomon et al.* [2001], i.e., multiplying the flux of photons for wavelengths below 25 nm by a factor of 4. The modeled photon flux, actually Earth values, is then scaled to Mars values by counting into the relative distance of both planets from the Sun. The cross-section information of photoionization and excitation for Mars environment used in the model is from *Fox* [1991], with an updated electron impact cross section from *Sung and Fox* [2000]. The neutral and ionospheric density profiles for Mars upper atmosphere are linearly interpolated from the Mars Thermospheric General Circulation Model (MTGCM) [*Bougher et al.*, 1988, 1994, 2001] within MTGCM's calculation domain from 100 km to 240 km. Above this altitude, both the neutral and electron densities are linearly extrapolated from the logarithm of the two topmost values from MTGCM.

3. Convergence Tests

In this section, convergence tests for the pitch angle grid, spatial grid, and energy grid have been conducted. Figure 1 shows the neutral density profiles of O, O_2, N_2, CO_2, CO, thermal electron density, and also neutral

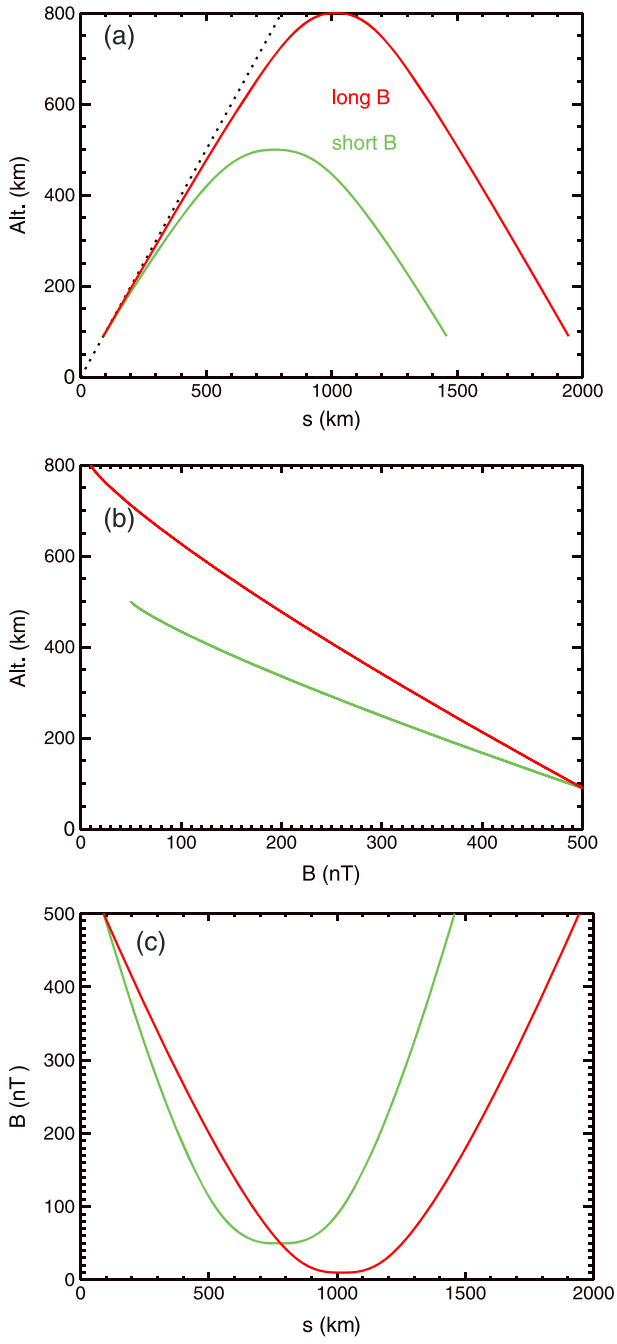

Figure 2. Two magnetic field configurations used in this study, the short *B* field line highlighted in green and the long *B* field line in red. (a) *B* field lines' altitude against distance *s* and the dotted line sketches a perfect vertical *B* field line; (b) *B* field strength against altitude; (c) *B* field strength against distance *s*.

temperature against altitude from MTGCM for the superthermal transport code. The MTGCM run was at an Ls of 90° with an Earth $F_{10.7}$ of 100.

If it is not specified, then the standard setup for this model is an Earth $F_{10.7}$ value of 100, 1.57 AU as the Sun-Mars distance to scale the modeled Earth EUV fluxes, and a constant energy step of 1 eV for the range 0.5–200.5 eV. Also, the solar zenith angle is set as 10°. For this study, symmetric closed *B* field lines, as shown in Figure 2, and the same background atmosphere and illumination for the two legs of the *B* fields are given. Because of the symmetry, only results of photoelectrons flowing in the "+*s*" direction (i.e., from $s=0$ km to maximum *s*) are shown in the following sections. That is, the electron fluxes in the $+s$ direction look identical to those in the $-s$ direction at an equivalent distance from the source region. While the distance variable *s* starts at $z=0$, the calculation does not start at the surface of the planet, rather it starts at $z=90$ km in the simulations presented below. Furthermore, for the case of precipitating electrons along an open field line, the calculation can start at the top of the simulation domain where the source of the particles is applied. Note that there are other "standard" field line configurations at Mars, namely, open lines connected to both Mars and the solar wind and draped solar wind field lines. They will not be examined here because the primary difference is the boundary condition.

These runs are steady state with a time step set to be 10^5 s, approximately 1 day, so large that the $\partial/\partial t$ term is mostly negligible. The convergence criteria is $|\psi-\psi_{\text{last}}|/\psi<0.01$, where ψ and ψ_{last} are the electron flux at the current time step and the last time step. However, the STET model is capable of simulating time dependence cases, simply setting the time step to an appropriately small value so that the $\partial/\partial t$ term plays a role, and has been applied to Earth space environment [e.g., *Liemohn*, 1997]. The time-dependent simulations for Mars environment are planned as the future work.

3.1. Pitch Angle Grid

Two different field line configurations, a short *B* field line (green) and a long *B* field line (red), are shown in Figure 2; Figures 2a and 2b for distance *s*, and *B* strength against altitude and Figure 2c for *B* strength

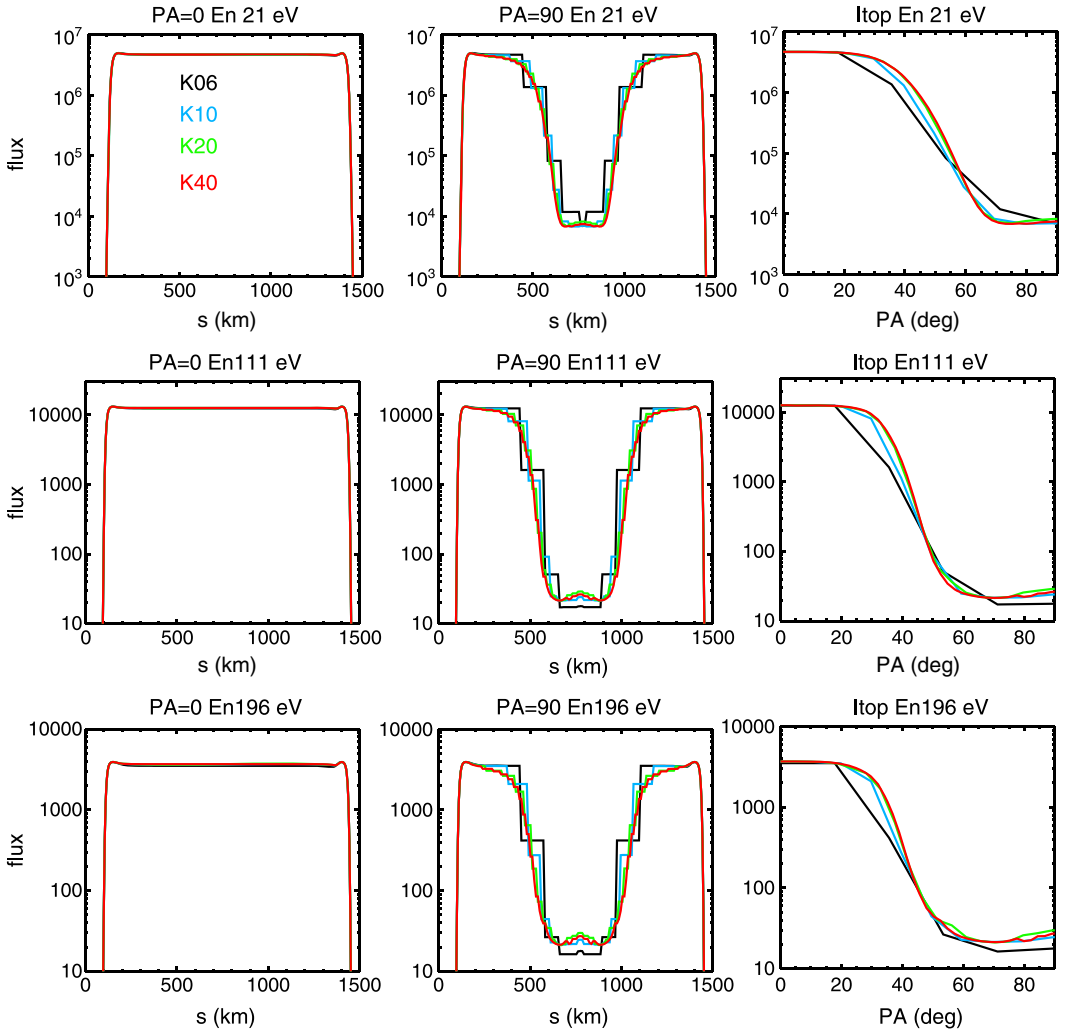

Figure 3. Results of different total pitch angle grid number, 6, 10, 20, and 40, highlighted in black, light blue, green, and red, respectively, in each plot. Three rows are for three energies: 21 eV, 111 eV, and 196 eV. (left and middle columns) The differential number flux (cm^{-2} s^{-1} eV^{-1} sr^{-1}) at PA = 0° and 90°, respectively, against distance *s*. (right) The differential number flux (cm^{-2} s^{-1} eV^{-1} sr^{-1}) against pitch angle at the top of the *B* field line.

against distance *s*. For the pitch angle grid convergence test, the short *B* field line will be used. The distance step size d*s* is 5 km below 200 km to well resolve the ionosphere and 10 km above this altitude. Also, the dotted line in Figure 2a marks the relationship for a vertical *B* field line for comparison.

As said in section 2, the calculation is in "$\mu_0 - s$" space instead of "pitch angle-*s*'' space, the transformation from pitch angles to μ_0 is not only as a function of cosine but also determined by the local magnetic strength relative to the minimum magnetic field strength. This nonlinear transformation, although providing advantages described in the section 2, makes the pitch angle grid setup not so straight forward. A constant μ_0 grid was tested but yields very large θ_0 spacing in the high-*B*-field ionospheric source region of the photoelectrons. To ensure several pitch angle grid steps in the ionosphere, therefore, a different approach was used. The pitch angle (PA) grid is set up as such a uniform minimum-*B* pitch angle θ_0 for all grid points except for the last pitch angle step size. The last PA step size is calculated as $\Delta\theta_0(\text{top}) = 90° - \sin^{-1}(\sqrt{B(s_{\text{top}})/B(s_{\text{top}-1})})$, i.e. the difference of 90° and θ_0 at the second to the top location ($\theta_0(s_{\text{top}} - 1) = \sin^{-1}\left(\sqrt{B(s_{\text{top}})/B(s_{\text{top}-1})}\right)$). The exception of the last pitch angle step size is to ensure the grid number K increase is no larger than 1 for the top *s* grid, which otherwise not only is a waste of grids but also can cause numerical issues. To calculate the pitch angle step sizes, take a total of 10 grid points as an example, it is $x \times (10-1) + 1° = 90°$, where 1° is the last step size. In this case, $x = 9.9°$. Four different total pitch angle grid numbers, 6, 10, 20, and 40, are tested. For this particular *B* field line, it is translated into the

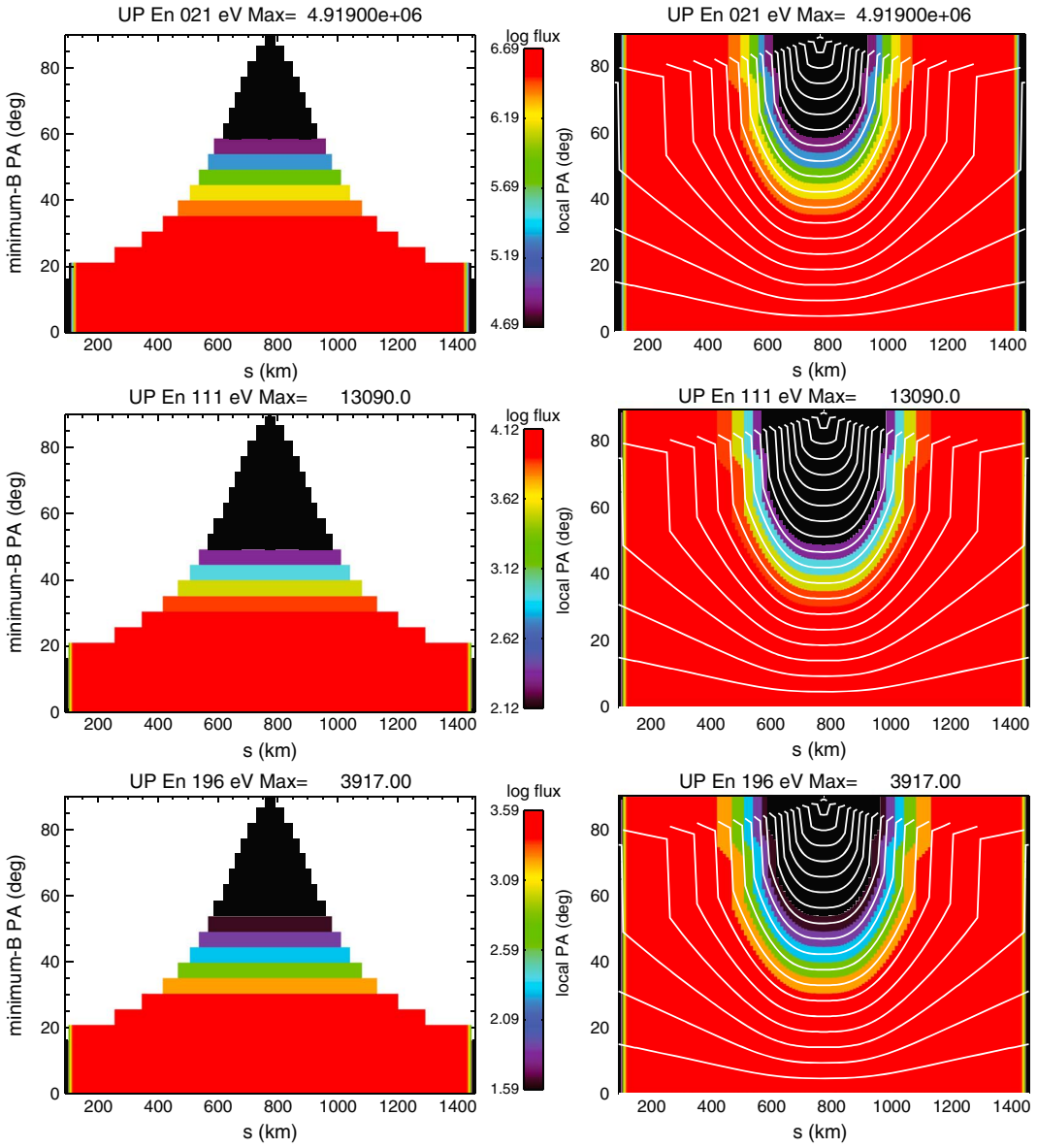

Figure 4. Pitch angle distributions along the whole *B* field for the run with a total pitch angle grid number of 20. Three rows again are for three energies: 21 eV, 111 eV, and 196 eV. (left column) The minimum-*B* pitch angle distribution. (right column) The local pitch angle distribution. The color shows the differential number flux in log scale, with a range from the maximum flux to 2 orders of magnitude smaller, and the white lines in the right column mark the same minimum-*B* PA.

uniform minimum-*B* pitch angle step size of θ_0 of 17.8°, 9.9°, 4.7°, 2.3°, respectively, and also 1.0° for the last step size.

The results are shown in Figure 3. The three rows are for three energies: 21 eV, 111 eV, and 196 eV. Figures 3 (left column) and 3 (middle column) are the differential number flux at local PA = 0° and 90°, respectively, against distance *s*. For Figure 3 (left column), the differential number fluxes are almost the same, unaffected by the different total pitch angle grid numbers. The fluxes first increase rapidly, mostly because of the source production by photoionization in the neutral atmosphere, then decrease slightly at s ~200 km due to the decreased source and loss processes, such as scattering, and slightly increase again at s ~1300 km caused by the source production in the other ionosphere. For the middle column (local PA = 90°), the fluxes are now influenced by the pitch angle grid size and converge as the grid step size is reduced. Figure 3 (right column) shows the differential number flux against pitch angle at the top of the *B* field line. The pitch

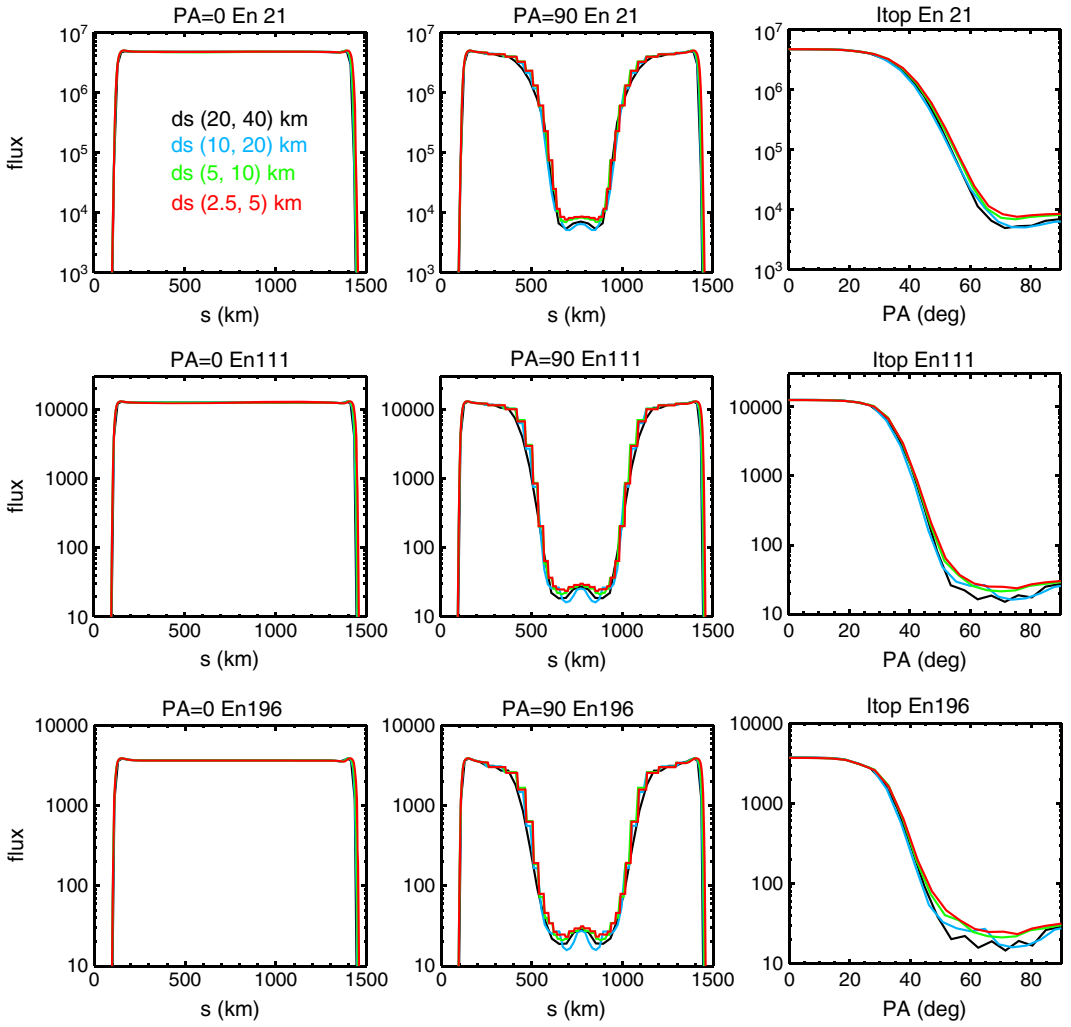

Figure 5. Results of different *s* grid size combinations, (20, 40), (10, 20), (5, 10), and (2.5, 5) (in kilometers), highlighted in black, light blue, green, and red, respectively, in each panel. Three rows are for three energies: 21 eV, 111 eV, and 196 eV. (left and middle columns) The differential number flux (cm^{-2} s^{-1} eV^{-1} sr^{-1}) at local PA = 0° and 90°, respectively, against distance s. (right column) The differential number flux (cm^{-2} s^{-1} eV^{-1} sr^{-1}) against pitch angle at the top of the *B* field line.

angle distributions are the typical source-cone distribution (high fluxes at PAs near 0° and low fluxes at PAs near 90°). Figures 3 (left column) and 3 (right column) show that with decreased pitch angle grid size, the flux distribution is more smooth and that a grid number of 10 is needed to resolve the pitch angle grid.

The example of a pitch angle distribution at each distance step with a total pitch angle grid of 20 is shown in Figure 4. Three rows are for three energies: 21 eV, 111 eV, and 196 eV. Figure 4 (left column) is the minimum-*B* pitch angle distribution, also an example of how the grid is actually setup in the calculation domain, while Figure 4 (right column) shows the local pitch angle distribution. The white lines in the right column mark the same minimum-*B* pitch angles for different local pitch angles at each *s* location. The pitch angle distribution is quite isotropic for altitudes lower than 350 km, corresponding to $s < 400$ km and > 1150 km, and rapid drop of fluxes at PA near 90° happens at higher altitudes due to the conservation of the first adiabatic invariant.

3.2. *S* Grid

With the knowledge of an appropriate pitch angle step size, the next step is to test the *s* grid of the short *B* field line with a total PA grid number of 20, although the pitch angle grid size changes slightly according to the last *s* grid step, which determines the last pitch angle grid step size. To ensure the ionosphere is well

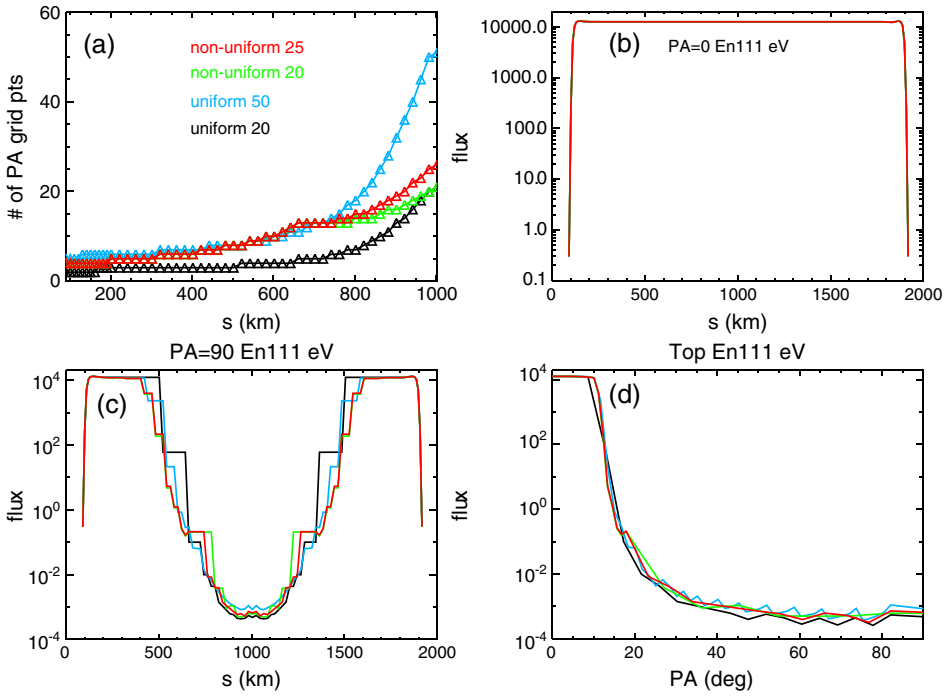

Figure 6. (a) Number of pitch angle grid points at each altitude. Black and blue lines are for uniform pitch angle grid setup with a total grid number of 20 and 50, respectively. The green and red lines are for nonuniform pitch angle grid setup with a total grid number of 20 and 25, respectively. (b) and (c) show the differential number flux (cm^{-2} s^{-1} eV^{-1} sr^{-1}) at PA = local 0° and 90°, respectively, against distance s. (d) shows the differential number flux (cm^{-2} s^{-1} eV^{-1} sr^{-1}) against pitch angle at the top of the *B* field.

resolved, the *s* grid step size under altitude of 200 km is half of that above 200 km. The results of the four combinations of *s* grid step size, (20, 40), (10, 20), (5, 10), and (2.5, 5) (in kilometers), are shown in Figure 5. The corresponding PA grid step sizes are, (4.47°, 5.1°), (4.62°, 2.2°), (4.68°, 1.0°), (4.72°, 0.3°), the former numbers for 19 uniform PA step size and the latter for the last step size. Similar to Figure 3, the three rows of Figure 5 are for three energies: 21 eV, 111 eV, and 196 eV.

Figure 5 (left column) and 5 (middle column) are the differential number flux at local PA = 0° and 90°, respectively, against distance *s*. These are not pitch angle distributions at a given altitude but rather flux values a constant local pitch angle value as a function of altitude. In Figure 5 (middle column), which shows the altitude profile of fluxes for the locally mirroring pitch angle, note that the finer spatial resolution results have a stair-step profile at high altitudes while the coarser spatial resolution results appear to be smoother at these altitudes (e.g., compare the red and black curves). This is because of the relationship between the spatial and pitch angle grids due to the changing magnetic field strength along the field line. Because these simulations were conducted with a fixed configuration for the minimum-*B* pitch angle steps, the addition of more spatial grid points along the field line results in several spatial locations with the same Ko(i) (i.e., number of minimum-*B* pitch angle steps for that i_{th} spatial location). Because transport dominates at the higher altitudes, the lowest altitude for a particular Ko(i) value will dominate the flux level, as seen by the nearly constant flux values for each K increment in Figure 4 (left column). This results in a stair-step profile for the PA = 90° flux values. For coarser spatial step sizes at high altitudes, Ko(i) will increment more often, perhaps with every spatial step, resulting a smoother altitude profile for the locally mirroring fluxes. Figure 4 (right column) shows the differential number flux against pitch angle at the top of the *B* field line. While all the lines are mostly on top of each other, the smaller *s* step size leads to a smoother pitch angle distribution at the top of the *B* field lines for trapped pitch angles (PA ~ 90°). Overall, the results suggest that the fluxes are not quite sensitive to the *s* grid step sizes. However, it does make sense to have *s* grid step size smaller than local-scale heights of the neutral species at Mars.

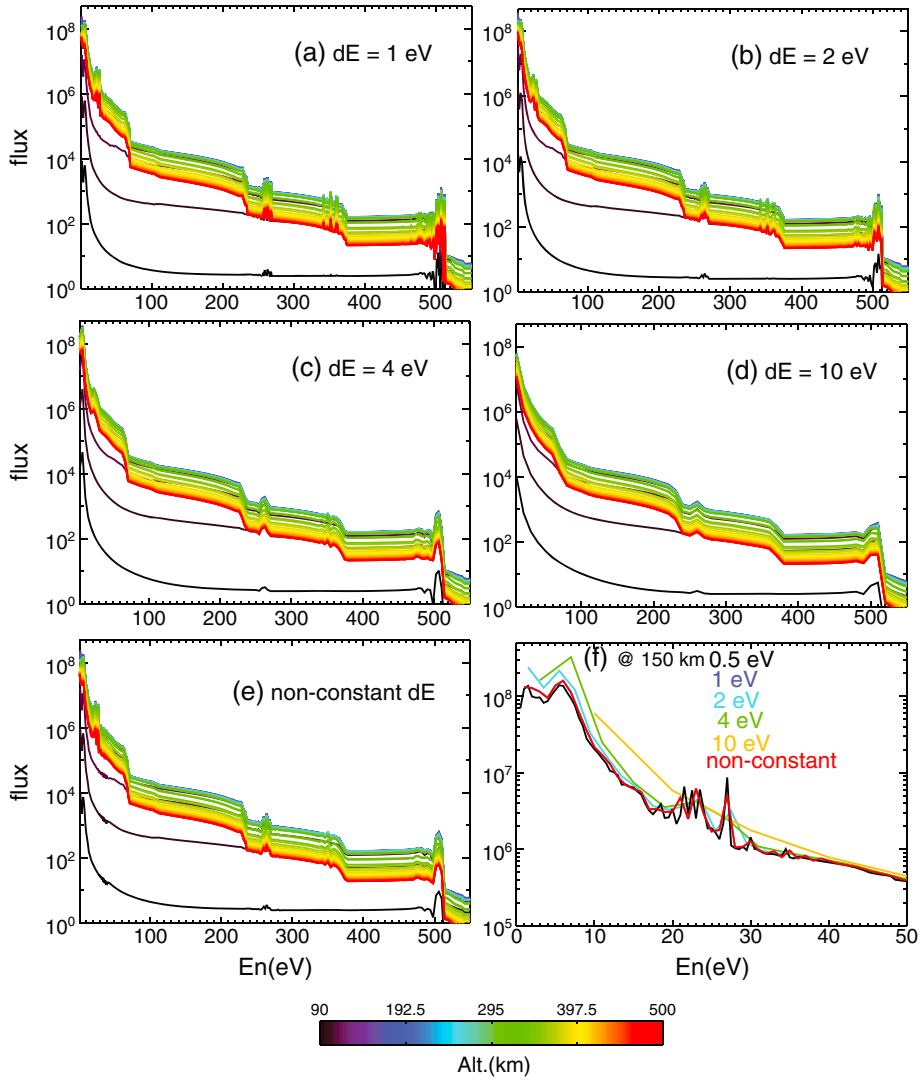

Figure 7. (a–d) The omnidirectional differential number flux against energy for a constant energy grid size with grid sizes of 1 eV, 2 eV, 4 eV, and 10 eV, respectively. Different colors highlight the energy spectra at different altitudes, as shown in the color bar. (e) The results of a nonconstant energy grid size. (f) The energy spectra at the altitude of 150 km from 0 eV to 50 eV. Results of the four uniform energy grid sizes of 1 eV, 2 eV, 4 eV, 10 eV and the nonconstant energy grid size are colored in blue, light blue, green, yellow, and red, respectively. In addition, the result of a run with energy grid size of 0.5 eV is highlighted in black.

3.3. Different Magnetic Field Configurations

The tested magnetic field in section 3.2 belongs to the relatively short field lines among the Martian strong crustal fields. Hence, another B field with a more extended altitude and a larger ratio of B strength maximum and minimum is also tested, as shown in red in Figure 2. The s step size is 10 km below 200 km and 20 km above. Because of this larger B maximum and minimum ratio, the uniform pitch angle step size setup described in section 3.1 has its disadvantages because of the complicated transformation from pitch angles to μ_0. The number of PA grid points at each altitude for this PA setup is shown in Figure 6a, black for a total PA grid points of 20 and light blue for 50. It is easy to see that, for $s < 600$ km (altitude below 570 km), only less than one third of the total PA grid points are utilized, resulting into rather coarse pitch angle resolutions in these altitudes.

Hence, the code is provided with another pitch angle grid setup. If $\theta_0(200)$ is the minimum-B pitch angle at 200 km, then from the minimum altitude to 200 km, K_1 of pitch angle grid points is assigned to this region and the pitch angle step size is $\theta_0(200)/K_1$. The second region is set up as such, from $\theta_0(200)$ to $2 * \theta_0(200)$ with K_2, so that the pitch angle step size is $\theta_0(200)/K_2$. Given K_4 is 1 for the last pitch angle step size with the

same setting as the shorter B field line. K_3 is $K_{total} - (K_1 + K_2 + K_4)$, accounting for minimum-B pitch angles from $2 * \theta_0(200)$ to $\theta_0(s_{top} - 1)$, where $\theta_0(s_{top} - 1)$ is θ_0 at the second to the top location. Here denote this method as the "nonuniform" PA grid setup. Two pitch angle grids of this nonuniform setup are shown in Figure 6a, green for a total pitch angle grid points of 20 and red for 25, with (2.24° , 1.1° , 9.1° , and 7.9°) and (4, 8, 7, and 1) and (2.24° , 1.1° , 5.4° , and 7.9°) and (4, 8, 12, and 1) for $\Delta\theta_0(1-4)$ and K_{1-4}, respectively. The only difference between the two is the K_3.

The results of two uniform PA grid setup and two nonuniform PA grid setup are shown in Figures 6b–6d, energy 111 eV as an example. Figures 6b–6d are the differential number flux at PA 0° and 90° against distance s, and the differential number flux at the top of the B field against pitch angle, respectively. In Figure 6c, two runs (black and light blue) with uniform PA grid setup are chunky between s 300 and 600 km while both runs (green and red lines) with the nonuniform setup are of a much finer resolution, even better than uniform PA grid setup with 50 grid points. For $600 < s < 1000$ km, the nonuniform setup provides the same as or slightly coarser resolution than the uniform setup. At the maximum altitude, the pitch angle distribution (Figure 6d) of all the runs are about the same. In all, this nonuniform pitch angle grid setup not only provides a good resolution with much fewer grid points but also some freedom to obtain the desired grid resolution at some particular regions according to the specific configuration of a magnetic field line.

Since section 3.2 already shows that the results are somehow insensitive to s grid step size, the test of s grid is skipped here.

3.4. Energy Grid

The last grid that needs to be tested is the energy grid, which is independent of B field configuration. Hence, the short B field, shown in green in Figure 2, is chosen to carry out the convergence test, with a PA grid setup the same as the case of a total PA grid number of 20 in section 3.1 and s grid setup of (10, 20) km. Four uniform energy grid sizes of 1eV, 2 eV, 4 eV, and 10 eV are used, with the results shown in Figures 7a–7d, respectively. Typical features of photoelectron energy spectra, such as the large flux drop near 60 eV due to the sharp drop in solar photons below 15 nm, the spikes near 270 eV and 500 eV due to Auger (inner shell) electron production by soft X-rays, and the abrupt cutoff around 500 eV as the extreme small source term beyond the last Auger peak, are seen in Figures 7a–7d [e.g., *Nagy and Banks*, 1970; *Mantas and Hanson*, 1979; *Liemohn et al.*, 2003]. The flux spikes in the 20–30 eV range due to the intense He II 30.4 nm solar line and also Auger peaks near 360 eV can only be identified in finer resolutions, below 4 eV, i.e., Figures 7a–7c.

The results above suggest that the determination at whether an energy grid size is sufficient highly depends on the question being asked and the energy range or feature being investigated. More than occasionally, especially for data-model comparisons, finer resolution in low-energy range is required and a relatively coarse resolution in high-energy range is acceptable. It is possible to set up the energy grid such that dE/E = consant. However, in order to have 1 eV grid resolution at 25 eV, it puts a lot of grid points in the 1–10 eV energy range. This makes a dE/E based energy grid impractical. Hence, we designed and tested a nonconstant energy grid size as follows: 1 eV for energy below 40 eV, 2 eV for 40–200 eV, and 4 eV for energy above 200 eV, with the results shown in Figure 7e. Flux spikes in the 20–30 eV range, Auger peaks near 270 eV and 360 eV and other features are easily identified. This energy grid setup also speeds up calculation due to fewer energy grid steps.

To more clearly show the structures in the low-energy range for different energy grid sizes, the energy spectra in the energy range of 0–50 eV for the five energy grid setups at an altitude of 150 km are shown in Figure 7f. Results of the four uniform energy grid sizes of 1 eV, 2 eV, 4 eV, and 10 eV and the nonconstant energy grid size are colored in blue, light blue, green, yellow, and red, respectively. In addition, a run with energy grid size of 0.5 eV, with a energy range of 0.25–200.25 eV, is also carried out to illustrate the finer structures of the photoelectrons in 0–50 eV range for comparison, highlighted in black in Figure 7f. Especially, in the 20–25 eV range, this black line shows three flux spikes, which smears into two with a step size of 1 eV. When the step size becomes coarser, the energy spectra is smeared further. In Figure 7f, the downside with the uneven energy grid size, however, is seen in the red line. Small oscillations occur just below the energy where the grid size changes, for example, near 30–40 eV, making the red line more spiky than the black line. With the technique used in *Swartz et al.* [1975] and a grid size change under a factor of 2, the oscillations are relatively small.

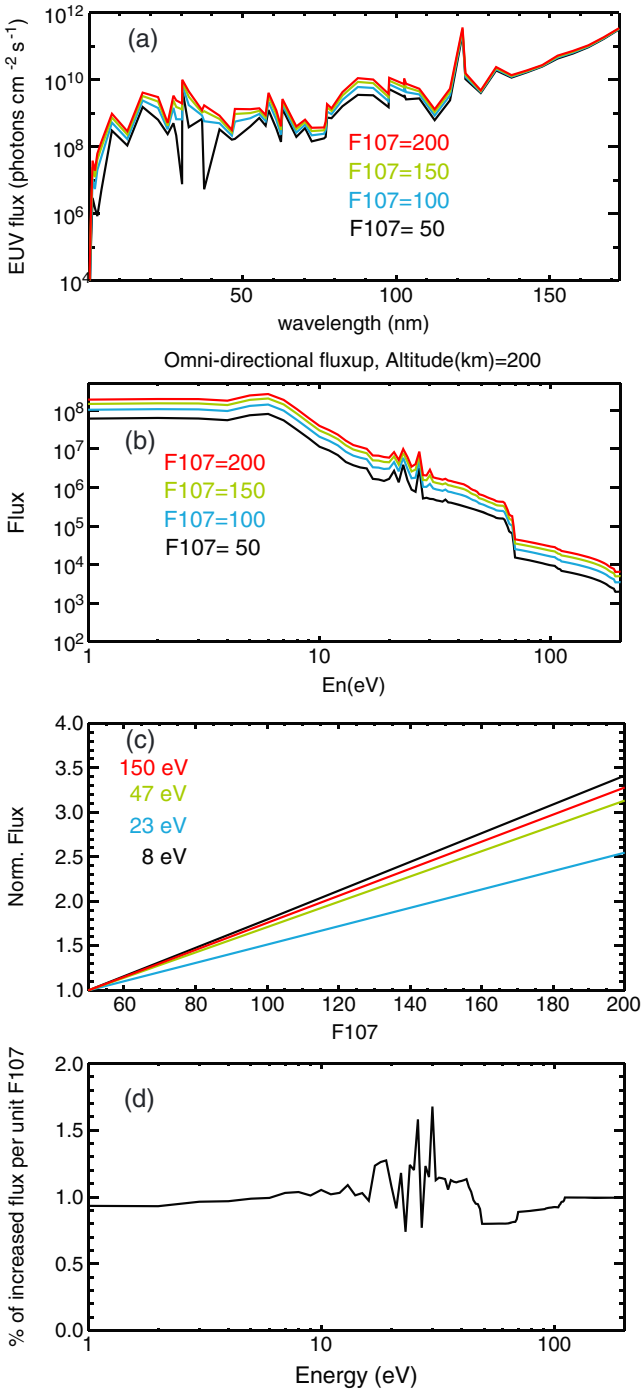

Figure 8. (a) Modeled EUV fluxes against wavelength, and different $F_{10.7}$ values at Earth are colored differently. (b) Omnidirectional differential number flux (cm^{-2} s^{-1} eV^{-1} sr^{-1}) against energy at altitude 200 km. For both Figures 8a and 8b, colors mark different $F_{10.7}$ cm inputs. (c) Normalized fluxes against $F_{10.7}$ values and four example energies are highlighted in different colors. (d) Percentage of increased fluxes per unit $F_{10.7}$ against energy.

4. Results: Physical Parameters

With the appropriate PA, *s*, and energy grid setups determined in the previous section, to further validate the model, the next step is to examine the performance of the transport code with different physical parameters, specially $F_{10.7}$ values (section 4.1), thermal electron/plasma density (section 4.2), and neutral densities (section 4.3). The short *B* field line is used in this section, with *s* step size of (10, 20) km. The pitch angle grid setup is the same as the case of a total PA grid number of 20 in section 3.1. The energy grid is of a step size of 1 eV and a range of 0.5–200.5 eV.

4.1. $F_{10.7}$ Values

Solar photon fluxes incident onto Mars vary dramatically during a solar cycle and even a Martian year. Hence, four Earth $F_{10.7}$ values, 50, 100, 150, and 200, are chosen as input for the Hinteregger model and after being scaled to Mars values by multiplying a factor of $1/r^2$ (r is the Mars-Sun distance in astronomical unit, 1.57 in this study), the modeled EUV fluxes against wavelength are shown in Figure 8a, highlighted in black, blue, green, and red, respectively. Despite the Hinteregger EUV flux's linear dependence on $F_{10.7}$, each wavelength has its own scaling factor. As a result, the increase of EUV flux varies for different wavelengths, as the four lines are "tighter together" in some wavelengths than others. This feature of the Hinteregger model translates into different responses of photoelectron fluxes for different energies.

To demonstrate, Figure 8b shows the energy spectra of omnidirectional photoelectron flux for these four Earth $F_{10.7}$ inputs at 200 km altitude. The differences in flux between the lines are difficult to see, and so the normalized flux (by the fluxes with $F_{10.7}=50$) against $F_{10.7}$ values for several energies are shown in Figure 8c. From Figure 8c where different slopes are seen, the increase factors of fluxes, or the percentages of increased flux, per unit $F_{10.7}$ for all the energies are shown in Figure 8d. This percentage varies for different energies,

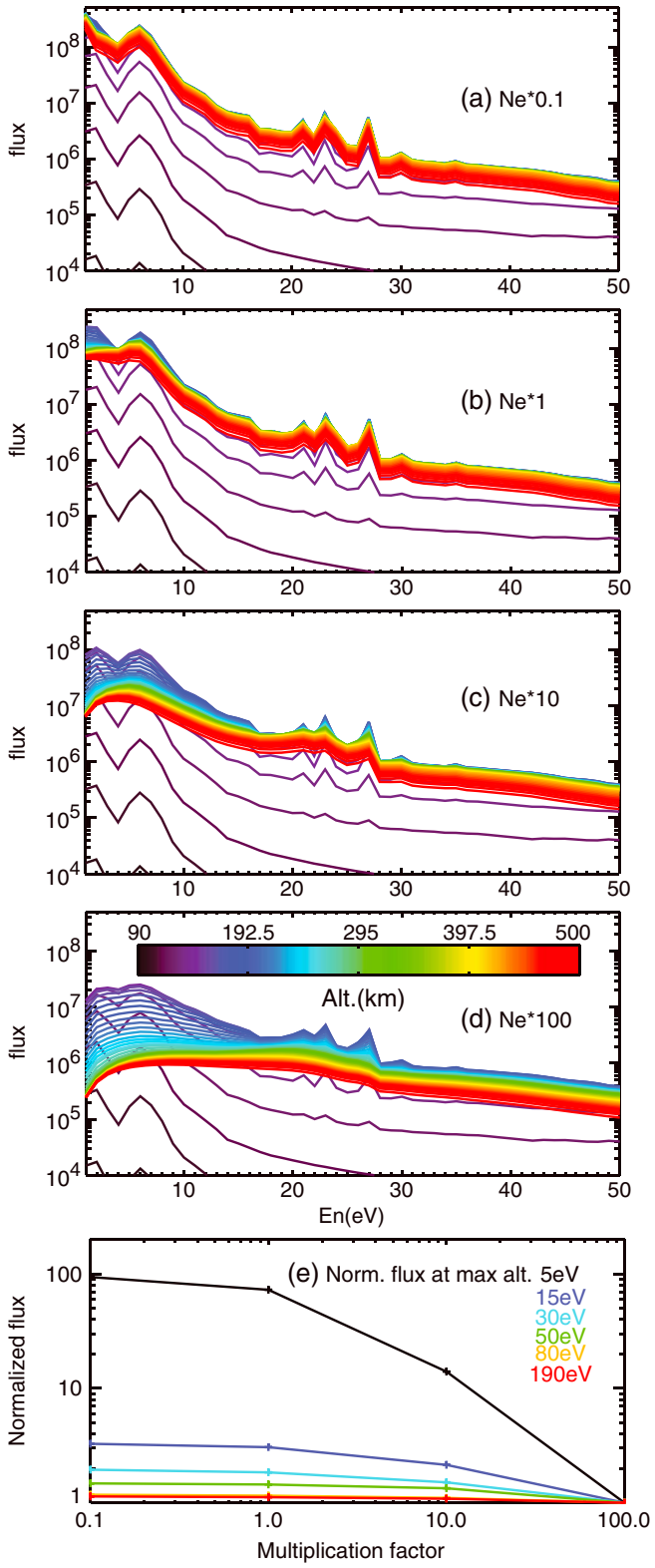

Figure 9. Omnidirectional differential number flux (cm^{-2} s^{-1} eV^{-1} sr^{-1}) against energy at different altitudes, marked by different colors. (b) For normal thermal electron density as shown in Figure 1. (a, c, and d) For this density scaled by a factor of 0.1, 10, and 100, respectively. (e) The normalized flux at the top of the magnetic field against the multiplication factor. Colors highlight different energies.

being especially spiky in the energy range of 20–30 eV. This variation produced by the transport code in the photoelectron fluxes is consistent with the Hinteregger EUV flux changing for different ionizating photon wavelengths.

4.2. Thermal Electron/Plasma Density

Thermal electron/plasma density is directly related to the loss of photoelectrons due to Coulomb collisions. To examine this effect, the normal electron density from MTGCM, shown as the black line in Figure 1, is scaled by a factor 0.1, 1, 10, and 100, and the resultant energy spectra are shown in Figures 9a–9d, respectively.

When electron density increases (Figures 9c and 9d), the omnidirectional fluxes at the top of the field line (colored in red) decrease more compared to the normal electron density (Figure 9b), especially in lower energies. It is due to the factor that the Coulomb collisional cross section is proportional to the inverse of squared energy ($1/E^2$). Also, the flux spikes in the 20–30 eV range are more degraded and barely seen at the top of the field line in Figure 9d.

When electron density decreases (Figure 9a), while the high-altitude flux drops is not as severe at the very low energies (below 10 eV), the results closely resemble the normal case. It hints that the loss due to Coulomb collision plays a relatively minor role compared to other loss mechanisms, i.e., elastic and inelastic collisions with neutral particles; hence, this reduced minor factor barely influences the final fluxes.

To quantitatively determine the photoelectron flux change caused by the different plasma densities, Figure 9e shows the normalized flux at the top of the magnetic field against the multiplication factor. For high energies, the photoelectron flux is barely affected due to the small Coulomb collision cross section. For really low energies (e.g., 5 eV),

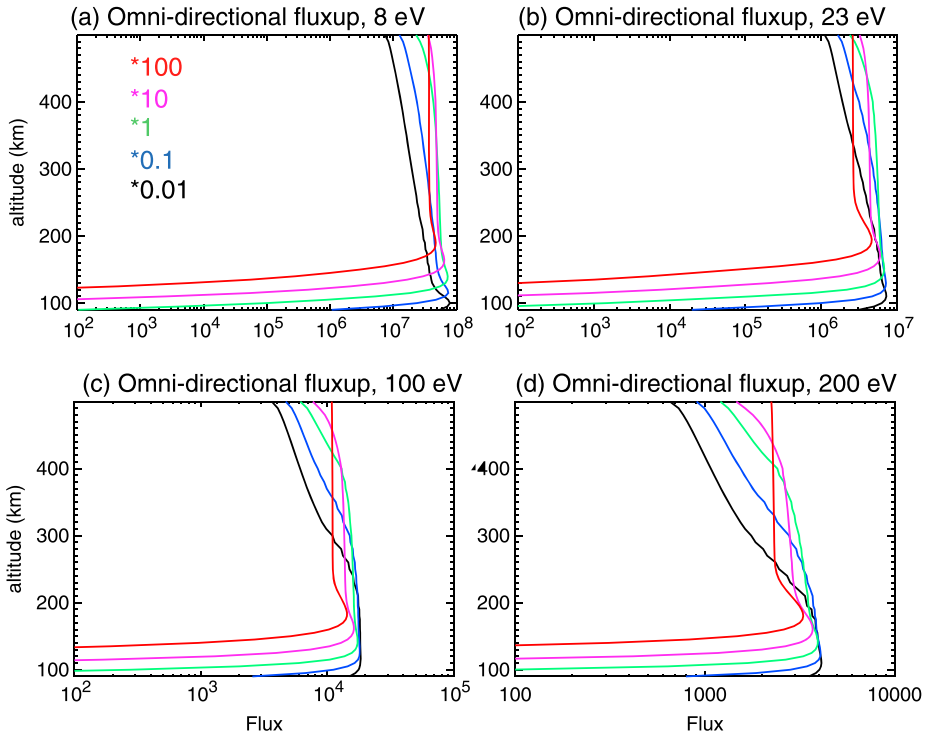

Figure 10. Omnidirectional differential number flux (cm^{-2} s^{-1} eV^{-1} sr^{-1}) against altitude for different energies, (a) 8 eV, (b) 23 eV, (c) 100 eV, and (d) 200 eV. In each plot, different colors are for the results of different neutral densities. Green is for normal neutral densities as shown in Figure 1. Black, blue, pink, and red are for neutral densities of all species scaled by a factor of 0.01, 0.1, 10, and 100, respectively.

photoelectron flux decreases almost linearly with the increase of the plasma density but barely changes with the decrease of the plasma density as the loss due to the Coulomb collision is small compared to other processes.

4.3. Neutral Densities

Neutral densities' effects on photoelectron fluxes are more complicated as they contribute to both the source and the loss. An easy way to validate the transport model's performance is to examine the electron flux peak altitude. According to Chapman theory [*Chapman*, 1931a, 1931b], when neutral density increases, as the solar EUV flux is absorbed more in the upper atmosphere and the optical depth reaches 1 at a higher altitude, the altitude of the peak electron flux also increases.

The densities of five neutral species are scaled by a factor of 0.01, 0.1, 1, 10, and 100, results colored in black, blue, green, pink, and red in Figure 10, respectively. Each panel is the omnidirectional flux against altitude for a particular energy. For all four panels, the peak altitude increases with elevated neutral densities. The peak fluxes tend to decrease a little as neutral densities increase but are mostly within 50% of each other. It might be partially due to the increased neutral temperature at the peak, as the neutral temperature increases with altitude in the Martian thermosphere, as shown in Figure 1 (the red line), and the peak altitudes for higher density cases increase as well. The resultant increased scale heights (H) lead to a decreased peak production rate ($\propto 1/H$) according to the Chapman theory (for example, see *Schunk and Nagy* [2000], equation (9.23)). In addition, the flux decreases less from the peak to the top of the field line as the neutral density increases, providing an increased source at high altitudes.

5. Data-Model Comparison

To further validate the STET model, the data-model comparison is performed here. The data chosen is from the magnetometer/electron reflectometer (MAG/ER) instrument on board Mars Global Surveyor (MGS) [*Acuña et al.*, 1998; *Mitchell et al.*, 2001]. The detailed description of the instrument is given in *Acuña et al.* [1992]. To isolate dayside photoelectron measurements over the strong crustal field regions, the same

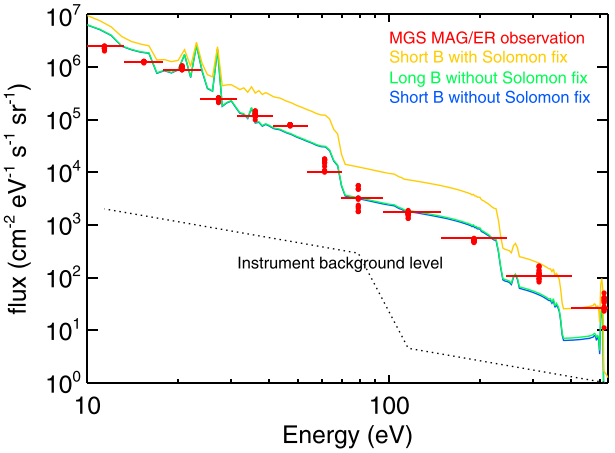

Figure 11. Omnidirectional flux against energy. The width of the solid red lines shows the energy resolution of the electron instrument and the red dots are the serial measurements from 03:48:27 to 03:48:59, 17 in total. The black dashed line is the instrument background level flux. The solid lines are the model results with the short and long *B* field line in Figure 2. The blue and green lines are the model runs of Hinteregger 81 without the Solomon fix, for the short and long field line, respectively. The yellow line is the model run of Hinteregger 81 with the Solomon fix for the short *B* field line.

method is applied as was done by *Xu et al.* [2014a]. To briefly summarize their method, a spatial constraint of 160°–200° east longitude and 30°–70° south latitude is applied, along with a magnetic field magnitude minimum constraint (35 nT), to ensure data selected over the strong crustal fields. In addition, to avoid solar wind electron precipitation through open magnetic field (more likely to be vertical at 400 km [e.g., *Xu et al.*, 2014b]), only absolute elevation angles (angles relative to the planet surface) within ± 45° are included. An orbit on 7 November 2005, 03:48:27 to 03:48:59, is chosen as the Sun, Earth, and Mars aligned so that the solar flux can be directly scaled from Earth to Mars by their relative solar distance. The spacecraft was at local time 2 P.M., south latitude ~ 46°, east longitude ~ 190°, and solar zenith angle ~ 37°. The magnitude of magnetic field is around 200 nT and the magnetic elevation angle, angle relative to the planet surface, is from 0 to 30°. For the model setup, the nonconstant energy grid setup described in section 3.4 is used. Earth $F_{10.7}$ and the relative Sun-Earth and Sun-Mars distances are given accordingly. The two magnetic field configurations shown in Figure 2 are both tested here. For the short *B* field line, a total pitch angle number of 20 is used, while for the long *B* field line, the nonuniform setup with 25 pitch angle grid points, as described in section 3.3, is employed.

The data-model comparison of the omnidirectional flux at MGS altitude (~400 km) is shown in Figure 11. The width of the solid red lines shows the energy resolution of the electron instrument and the red dots are the serial measurements from 03:48:27 to 03:48:59, 17 in total. The yellow line is the model run of Hinteregger 81 with the Solomon fix [*Solomon et al.*, 2001] for magnetic field line *B*2. Compared with the MGS observation, the model result matches with the data above 300 eV and is 2–4 times higher for energy below 200 eV. The Solomon fix is to multiply the EUV flux below 25 nm from Hinteregger 81 model by 4. Then, a model run of Hinteregger 81 without the Solomon fix for the short magnetic field line is shown in blue line in Figure 11. Now the modeled results matches well with the observation, within a factor of 2 below 200 eV. The disagreement at energy bin 61 eV, right around the large flux drop, is probably due to the spacecraft potential shift, resulting into mixing electron fluxes of this bin with its neighbor bins and smearing the flux drop. In addition, another discrepancy between the model and the data is the flux spikes in 20–30 eV range, which are missing from the data. It may be caused by the coarse resolution ($\Delta E/E = 25\%$) of the instrument and/or the discrepancy between the modeled EUV fluxes and the actual values.

The model result, without the Solomon fix, with the long *B* field line, is also shown in Figure 2, highlighted in green. As can be seen in Figure 11, the magnetic field description had essentially no influence on the photoelectron omnidirectional flux values at 400 km altitude. While the magnetic field topology is important for electron transport and the details of the pitch angle distribution, Figure 11 shows that it is relatively unimportant for this pitch angle averaged quantity. The disagreements between our model results and the observations are within a factor of 2. Especially, solar EUV flux directly controls photoelectron fluxes and the EUV photon intensities from the Hinteregger-81 model may be off from the actual solar EUV by different factors at different wavelengths, which could introduce a significant different discrepancy at different energies. In addition, both neutral density and field line configuration discrepancies tend to introduce a systematic decrease/increase of fluxes for all energies. More detailed assessments of the factors controlling photoelectron fluxes at Mars will be the subject of future studies. Despite the fact that the two magnetic configurations are of different lengths, minimum and maximum ratios, the model results are almost iden-

tical, suggesting the high-altitude photoelectron omnidirectional fluxes are somewhat insensitive to the magnetic fields. However, as the two tested field lines are symmetric, an extremely asymmetric field line, such as an open field line, can lead to the decrease of omnidirectional flux by a factor less than three for transport dominant altitudes [e.g., *Mantas and Hanson*, 1979].

6. Discussion and Conclusions

In the previous sections, a numerical model for superthermal electron transport has been described in detail. This nonsteady state multistream transport model includes important physical processes such as energy degradation, pitch angle focusing, pitch angle diffusion, and field-aligned transport and is competent to simulate the complex Martian environment.

This study consists of three parts: the convergence tests, the physical parameters tests, and the data-model comparison. The step size of three variables, pitch angle, s, and E, have been examined. Because the calculation is in s-μ_0 space, the pitch angle grid and s grid are related. As a result, two methods to set up the pitch angle grid are introduced: a uniform step size of the minimum-B pitch angle θ_0 accompanied with the specified last step size, which is the difference of 90° and θ_0 at the second to the top location; a grid setup by dividing the ionosphere into four regions (details in section 3.3). These two methods are well suited for small and large B_{max}/B_{min}, respectively, suggesting that the model is capable of simulating arbitrary magnetic fields. For the s grid, to ensure the source region of photoelectrons is well resolved, the s step size below 200 km in altitude is half of that above this altitude. Given the similar results from various s step size combinations, it appears that the code is more sensitive to pitch angle grid setup than the s grid step size. Finally, the energy grid, as an independent variable, is tested with various uniform step sizes. The resultant energy spectra show that while the step size of 1 eV is sufficient to capture fine structures, the suitable energy step size highly depends on the question asked, such as a finer resolution to identify finer flux spikes. It is often the case that a finer resolution for the low-energy range and coarser for the high-energy range is desirable, especially for data-model comparison. The results of such a nonuniform grid setup are ideal, except for small oscillations near where the grid step size changes.

The tests of three physical parameters, $F_{10.7}$ values, thermal electron/plasma density and neutral densities, not only show that the transport model can handle different inputs but also validate the performance of the model. First, an interesting fact about the Hinteregger model is that the photon flux of each wavelength is scaled differently. The resultant photoelectron fluxes also show a nonuniform percentage of increase. Second, the expected degradation of fluxes, especially in the low-energy range is also seen in the results when thermal electron/plasma density increases. Finally, when the neutral densities increase, the elevated peak altitude of photoelectron fluxes is expected and found, as the optical depth of 1 is at a higher altitude.

Finally, the data-model comparison is carried out in section 5. On one hand, the modeled omnidirectional fluxes are of better agreement with MGS MAG/ER data without Solomon fix [*Solomon et al.*, 2001] for energies below 200 eV but with Solomon fix for energies above 300 eV. It suggests that the current fix (multiplying by a factor of 4 for wavelength below 25 nm) may extend to much longer wavelengths than necessary and this correction might be only necessary for wavelength below a few nanometers. On the other hand, even though two very different magnetic configurations are given, the omnidirectional fluxes are about the same at 400 km. This preliminary finding hints that the high-altitude photoelectron flux is insensitive to symmetric magnetic fields to some degree. However, previous studies [e.g., *Mantas and Hanson*, 1979] have shown that the modeled escaped photoelectron fluxes differ by a factor below three for horizontal and vertical magnetic fields. In other words, the asymmetry of a magnetic field line varies the omnidirectional flux by a factor less than three.

With the appropriate step sizes of various variables determined and validated through several physical parameters and data-model comparisons, the transport model performs well in this study but has plenty of room to improve. For example, it does not include wave-particle interactions, which might be needed to explain the more isotropic pitch angle distribution of superthermal electrons observed by Mars Global Surveyor [e.g., *Liemohn et al.*, 2003; *Brain et al.*, 2007]. In addition, there are several other EUV flux models, such as the Flare Irradiance Spectral Model [*Chamberlin et al.*, 2007, 2008], which are planned to be implemented into the transport model. Other magnetic configurations could also be examined, such as open or draped field lines. Finally, another future task involves case scenarios where nonsteady state

simulations should be employed, such as the evolution of the electron fluxes at the trapped zone pitch angles at the top of the closed magnetic fields.

Even though this study focused on the usage of STET for the Mars space environment, the code is fully capable of simulating electrons along any magnetic field line in any space physics application. For instance, it has been used extensively for Earth electron transport [e.g., *Khazanov and Liemohn*, 1995; *Khazanov et al.*, 2013]. It could be applied to other planetary space environments, like the draped solar wind fields at Venus, the auroral regions of Jupiter and Saturn, and the footpoints of moons at the outer planets. Yet another usage of the code could be simulating solar wind electron strahl or halo distributions.

Acknowledgments
The authors would like to thank NASA and NSF for their support of this project under grants NNX13AG26G and AST-0908311. The authors would also like to thank David Mitchell for providing MGS MAG/ER data. The numerical data and the current version of the SuperThermal Electron Transport (STET) model are available upon request to the authors. Most of the MGS MAG/ER data are archived in the Planetary Data System (PDS) and the full MGS MAG/ER dataset used in the paper is available upon request to David Mitchell (mitchell@ssl.berkeley.edu).

References

Acuña, M., et al. (1992), Mars observer magnetic fields investigation, *J. Geophys. Res.*, *97*(E5), 7799–7814.
Acuña, M., et al. (1998), Magnetic field and plasma observations at mars: Initial results of the Mars global surveyor mission, *Science*, *279*(5357), 1676–1680.
Bougher, S. W., R. E. Dickinson, R. G. Roble, and E. C. Ridley (1988), Mars thermospheric general circulation model—Calculations for the arrival of PHOBOS at Mars, *Geophys. Res. Lett.*, *15*, 1511–514, doi:10.1029/GL015i013p01511.
Bougher, S. W., D. M. Hunten, and R. G. Roble (1994), CO_2 cooling in terrestrial planet thermospheres, *J. Geophys. Res.*, *99*, 14,609–14,622, doi:10.1029/94JE01088.
Bougher, S. W., S. Engel, D. P. Hinson, and J. M. Forbes (2001), Mars Global Surveyor radio science electron density profiles: Neutral atmosphere implications, *Geophys. Res. Lett.*, *28*, 3091–3094, doi:10.1029/2001GL012884.
Brain, D., F. Bagenal, M. Acuña, and J. Connerney (2003), Martian magnetic morphology: Contributions from the solar wind and crust, *J. Geophys. Res.*, *108*(A12), 1424, doi:10.1029/2002JA009482.
Brain, D., R. Lillis, D. Mitchell, J. Halekas, and R. Lin (2007), Electron pitch angle distributions as indicators of magnetic field topology near Mars, *J. Geophys. Res.*, *112*, A09201, doi:10.1029/2007JA012435.
Chamberlin, P. C., T. N. Woods, and F. G. Eparvier (2007), Flare Irradiance Spectral Model (FISM): Daily component algorithms and results, *Space Weather*, *5*, S07005, doi:10.1029/2007SW000316.
Chamberlin, P. C., T. N. Woods, and F. G. Eparvier (2008), Flare Irradiance Spectral Model (FISM): Flare component algorithms and results, *Space Weather*, *6*, S05001, doi:10.1029/2007SW000372.
Chapman, S. (1931a), The absorption and dissociative or ionizing effect of monochromatic radiation in an atmosphere on a rotating earth, *Proc. Phys. Soc.*, *43*, 26–45, doi:10.1088/0959-5309/43/1/305.
Chapman, S. (1931b), The absorption and dissociative or ionizing effect of monochromatic radiation in an atmosphere on a rotating Earth. Part II. Grazing incidence, *Proc. Phys. Soc.*, *43*, 483–501, doi:10.1088/0959-5309/43/5/302.
Fillingim, M. O., L. M. Peticolas, R. J. Lillis, D. A. Brain, J. S. Halekas, D. L. Mitchell, R. P. Lin, D. Lummerzheim, S. W. Bougher, and D. L. Kirchner (2007), Model calculations of electron precipitation induced ionization patches on the nightside of Mars, *Geophys. Res. Lett.*, *34*, L12101, doi:10.1029/2007GL029986.
Fox, J. L. (1988), Heating efficiencies in the thermosphere of Venus reconsidered, *Planet. Space Sci.*, *36*(1), 37–46.
Fox, J. L. (1991), Cross sections and reaction rates of relevance to aeronomy, *Rev. Geophys.*, *29*, 1110–1131.
Fox, J. L., and A. Dalgarno (1979), Electron energy deposition in carbon dioxide, *Planet. Space Sci.*, *27*, 491–502, doi:10.1016/0032-0633(79)90126-0.
Fox, J. L., J. F. Brannon, and H. S. Porter (1993), Upper limits to the nightside ionosphere of Mars, *Geophys. Res. Lett.*, *20*, 1339–1342, doi:10.1029/93GL01349.
Gefan, G. D., and G. V. Khazanov (1990), Non-steady-state conditions of filling up the geomagnetic trap with superthermal electrons, *Ann. Geophys.*, *8*, 519–523.
Haider, S. A. (1997), Chemistry of the nightside ionosphere of Mars, *J. Geophys. Res.*, *102*, 407–416, doi:10.1029/96JA02353.
Haider, S. A., J. Kim, A. F. Nagy, C. N. Keller, M. I. Verigin, K. I. Gringauz, N. M. Shutte, K. Szego, and P. Kiraly (1992), Calculated ionization rates, ion densities, and airglow emission rates due to precipitating electrons in the nightside ionosphere of Mars, *J. Geophys. Res.*, *97*, 10,637–10,641, doi:10.1029/92JA00317.
Haider, S. A., S. P. Seth, E. Kallio, and K. I. Oyama (2002), Solar EUV and electron-proton-hydrogen atom-produced ionosphere on Mars: Comparative studies of particle fluxes and ion production rates due to different processes, *Icarus*, *159*, 18–30, doi:10.1006/icar.2002.6919.
Harnett, E. M., and R. M. Winglee (2005), Three-dimensional fluid simulations of plasma asymmetries in the Martian magnetotail caused by the magnetic anomalies, *J. Geophys. Res.*, *110*, A07226, doi:10.1029/2003JA010315.
Hinteregger, H. E., K. Fukui, and B. R. Gilson (1981), Observational, reference and model data on solar EUV, from measurements on AE-E, *J. Geophys. Res.*, *8*, 1147–1150, doi:10.1029/GL008i011p01147.
Khazanov, G. V. (1979), The kinetics of the electron plasma component of the upper atmosphere, [in Russian, English translation, National Translation Center, #80-50707, Washington, D. C., 1980], Moscow, Nauka.
Khazanov, G. V., and M. W. Liemohn (1995), Nonsteady state ionosphere-plasmasphere coupling of superthermal electrons, *J. Geophys. Res.*, *100*(A6), 9669–9681.
Khazanov, G. V., M. W. Liemohn, T. I. Gombosi, and A. F. Nagy (1993), Non-steady-state transport of superthermal electrons in the plasmasphere, *Geophys. Res. Lett.*, *20*, 2821–2824, doi:10.1029/93GL03121.
Khazanov, G. V., T. Neubert, and G. D. Gefan (1994), Unified theory of ionosphere-plasmasphere transport of suprathermal electrons, *IEEE Trans. Plasma Sci.*, *22*, 187–198, doi:10.1109/27.279022.
Khazanov, G. V., A. Glocer, M. W. Liemohn, and E. W. Himwich (2013), Superthermal electron energy interchange in the ionosphere-plasmasphere system, *J. Geophys. Res. Space Physics*, *118*, 925–934, doi:10.1002/jgra.50127.
Krymskii, A., T. Breus, N. Ness, D. Hinson, and D. Bojkov (2003), Effect of crustal magnetic fields on the near terminator ionosphere at mars: Comparison of in situ magnetic field measurements with the data of radio science experiments on board Mars global surveyor, *J. Geophys. Res.*, *108*(A12), 1431, doi:10.1029/2002JA009662.
Leblanc, F., O. Witasse, J. Winningham, D. Brain, J. Lilensten, P.-L. Blelly, R. A. Frahm, J. S. Halekas, and J. L. Bertaux (2006), Origins of the Martian aurora observed by Spectroscopy for Investigation of Characteristics of the Atmosphere of Mars (SPICAM) on board Mars Express, *J. Geophys. Res.*, *111*, A09313, doi:10.1029/2006JA011763.

Liemohn, M., G. Khazanov, T. Moore, and S. Guiter (1997), Self-consistent superthermal electron effects on plasmaspheric refilling, *J. Geophys. Res.*, *102*(A4), 7523–7536.

Liemohn, M. W. (1997), Self-consistent coupling of superthermal electrons with thermal plasma, PhD thesis, Univ. of Michigan.

Liemohn, M. W., D. L. Mitchell, A. F. Nagy, J. L. Fox, T. W. Reimer, and Y. Ma (2003), Comparisons of electron fluxes measured in the crustal fields at Mars by the mgs magnetometer/electron reflectometer instrument with a b field-dependent transport code, *J. Geophys. Res.*, *108*(E12), 5134, doi:10.1029/2003JE002158.

Liemohn, M. W., et al. (2006), Numerical interpretation of high-altitude photoelectron observations, *Icarus*, *182*(2), 383–395.

Lillis, R. J., D. L. Mitchell, R. P. Lin, and M. H. Acuña (2008), Electron reflectometry in the Martian atmosphere, *Icarus*, *194*, 544–561, doi:10.1016/j.icarus.2007.09.030.

Lillis, R. J., M. O. Fillingim, L. M. Peticolas, D. A. Brain, R. P. Lin, and S. W. Bougher (2009), Nightside ionosphere of Mars: Modeling the effects of crustal magnetic fields and electron pitch angle distributions on electron impact ionization, *J. Geophys. Res.*, *114*, E11009, doi:10.1029/2009JE003379.

Lillis, R. J., M. O. Fillingim, and D. A. Brain (2011), Three-dimensional structure of the Martian nightside ionosphere: Predicted rates of impact ionization from Mars Global Surveyor magnetometer and electron reflectometer measurements of precipitating electrons, *J. Geophys. Res.*, *116*, A12317, doi:10.1029/2011JA016982.

Ma, Y. J., X. Fang, A. F. Nagy, C. T. Russell, and G. Toth (2014), Martian ionospheric responses to dynamic pressure enhancements in the solar wind, *J. Geophys. Res. Space Physics*, *119*, 1272–1286, doi:10.1002/2013JA019402.

Mantas, G. P., and W. B. Hanson (1979), Photoelectron fluxes in the Martian ionosphere, *J. Geophys. Res.*, *84*(A2), 369–385, doi:10.1029/JA084iA02p00369.

Mitchell, D., R. Lin, C. Mazelle, H. Reme, P. Cloutier, J. Connerney, M. Acuña, and N. Ness (2001), Probing Mars' crustal magnetic field and ionosphere with the mgs electron reflectometer, *J. Geophys. Res.*, *106*(E10), 23,419–23,427.

Nagy, A. F., and P. M. Banks (1970), Photoelectron fluxes in the ionosphere, *J. Geophys. Res.*, *75*, 6260–6270, doi:10.1029/JA075i031p06260.

Rohrbaugh, R. P., J. S. Nisbet, E. Bleuler, and J. R. Herman (1979), The effect of energetically produced O_2^+ on the ion temperatures of the Martian thermosphere, *J. Geophys. Res.*, *84*, 3327–3338, doi:10.1029/JA084iA07p03327.

Schunk, R., and A. Nagy (2000), *Ionospheres: Physics, Plasma Physics, and Chemistry, Cambridge Atmos. Space Sci. Ser.*, vol. 59, 554 pp., Cambridge Univ. Press, Cambridge, U. K.

Seth, S. P., S. A. Haider, and K. I. Oyama (2002), Photoelectron flux and nightglow emissions of 5577 and 6300 Å due to solar wind electron precipitation in Martian atmosphere, *J. Geophys. Res.*, *107*(A10), 1324, doi:10.1029/2001JA000261.

Solomon, S. C., S. M. Bailey, and T. N. Woods (2001), Effect of solar soft X-rays on the lower ionosphere, *Geophys. Res. Lett.*, *28*, 2149–2152, doi:10.1029/2001GL012866.

Sung, K., and J. L. Fox (2000), Electron impact cross sections for use in modeling the ionospheres/thermospheres of the Earth and Planets, *Eos Trans. AGU*, *81*(48), Fall Meet. Suppl., Abstract SA52A-11.

Swartz, W. E., G. J. Bailey, and R. J. Moffett (1975), Electron heating resulting from interhemispherical transport of photoelectrons, *Planet. Space Sci.*, *23*, 589–598, doi:10.1016/0032-0633(75)90099-9.

Torr, M. R., P. Richards, and D. Torr (1980), A new determination of the ultraviolet heating efficiency of the thermosphere, *J. Geophys. Res.*, *85*(A12), 6819–6826.

Verigin, M. I., K. I. Gringauz, N. M. Shutte, S. A. Haider, K. Szego, P. Kiraly, A. F. Nagy, and T. I. Gombosi (1991), On the possible source of the ionization in the nighttime Martian ionosphere. I—PHOBOS 2 HARP electron spectrometer measurements, *J. Geophys. Res.*, *96*, 19,307–19,313, doi:10.1029/91JA00924.

Xu, S., M. W. Liemohn, D. L. Mitchell, and M. D. Smith (2014a), Mars photoelectron energy and pitch angle dependence on intense lower atmospheric dust storms, *J. Geophys. Res. Planets*, *119*, 1689–1706, doi:10.1002/2013JE004594.

Xu, S., M. W. Liemohn, and D. L. Mitchell (2014b), Solar wind electron precipitation into the dayside Martian upper atmosphere through the cusps of strong crustal fields, *J. Geophys. Res. Space Physics*, *119*, 10,100–10,115, doi:10.1002/2014JA020363.